



**HAL**  
open science

## Three-dimensional characterization of a fractured granite and transport properties

R. Gonzalez-Garcia, O. Huseby, J. -F. Thovert, B. Ledésert, P. M. Adler

► **To cite this version:**

R. Gonzalez-Garcia, O. Huseby, J. -F. Thovert, B. Ledésert, P. M. Adler. Three-dimensional characterization of a fractured granite and transport properties. *Journal of Geophysical Research : Solid Earth*, 2000, 105, pp.21,387-21,401. 10.1029/2000JB900149 . insu-03596931

**HAL Id: insu-03596931**

**<https://insu.hal.science/insu-03596931>**

Submitted on 4 Mar 2022

**HAL** is a multi-disciplinary open access archive for the deposit and dissemination of scientific research documents, whether they are published or not. The documents may come from teaching and research institutions in France or abroad, or from public or private research centers.

L'archive ouverte pluridisciplinaire **HAL**, est destinée au dépôt et à la diffusion de documents scientifiques de niveau recherche, publiés ou non, émanant des établissements d'enseignement et de recherche français ou étrangers, des laboratoires publics ou privés.

Copyright

## Three-dimensional characterization of a fractured granite and transport properties

R. Gonzalez-Garcia,<sup>1</sup> O. Huseby,<sup>2,3</sup> J.-F. Thovert,<sup>1</sup>  
B. Ledésert,<sup>4</sup> and P. M. Adler<sup>2</sup>

**Abstract.** A three-dimensional fracture network in a granite block is reconstructed from a series of experimental serial sections. It is visualized and its most important geometrical characteristics are studied, namely the orientation of the fractures, the connectivity of the fractures, the number of cycles, per unit volume, the distributions of surface areas and of the intersection lengths, and the number of finite solid blocks isolated in the solid matrix by the network. Though the network mostly consists of two families of fractures, it is interesting to note that a simple model of randomly oriented, monodisperse hexagons often yields a good order of magnitude for the various geometrical properties, which have been measured on the real block. The flow properties are then studied; examples of velocity field are provided as well as histograms of velocities; the permeability tensor is determined and is found to be in good agreement with Snow's formula. Finally, dispersion is analyzed by means of a random walk method; histograms of arrival times are provided and interpreted in terms of dispersion tensor.

### 1. Introduction

In most cases, the experimental data concerning geological fracture networks are obtained from one- or two-dimensional observations. Examples of borehole surveys are given by *Narr and Lerche* [1984] and *Genter et al.* [1995]. A variety of information can be obtained from core analysis, such as fracture density or spacing, or orientation statistics. However, these one-dimensional sections provide little information regarding the extension or the interconnectivity of the fractures.

Two-dimensional observations provide a much more realistic image of the fracture network. Sections of various extensions can be revealed in man-made excavations, such as tunnels or drifts [e.g., *Rouleau and Gale*, 1985; *Billaux et al.*, 1989; *Abelin et al.*, 1991], or quarries [e.g., *Gervais*, 1993]. They may also appear naturally in outcrops. Fracture trace maps can then be drawn at various scales of observation. For instance, *Odling* [1992] investigated a  $18 \times 18 \text{ m}^2$  area from ground observation, whereas *Barthélémy* [1992] and *Barthélémy et al.* [1996] used photographs shot from planes or he-

licopters, and *Vignes-Adler et al.* [1991] used satellite images. Unlike borehole surveys, these two-dimensional views provide information (at least partial) relative to fracture extensions and to their connectivity. Their in-plane orientation (strike) is also readily available, although the inclination (dip) is not. Fracture density can be measured by counting the number or the cumulated length of fracture traces per unit area.

Stereological techniques have often been applied to infer three-dimensional (3-D) information from 2-D trace maps. For instance, *Berkowitz and Adler* [1998] devised a solution algorithm to the inverse problem of determining the fracture size distribution from the trace length distribution. They also obtain analytical expressions for the fracture density, for the fracture intersection density, and for the intersection length distribution. However, this approach necessarily relies on a priori hypotheses such as the usual assumption that fractures can be treated as disks.

Very few attempts to fully characterize fracture networks in three dimensions have been reported in the literature for obvious practical reasons. Three-dimensional imaging techniques such as nuclear magnetic resonance, X-ray computed tomography (CT), and confocal microscopy are restricted to laboratory measurements on small samples because of their limited imaging field or penetration depth. For instance, *Montemagno and Pyrak-Nolte* [1995] and *Pyrak-Nolte et al.* [1997] imaged decimetric coal samples with a  $300 \mu\text{m}$  spatial resolution by X-ray CT. Three characterizations by serial sectioning can be mentioned, namely that of *Koestler and Reksten* [1992] at a decametric scale in a quarry, and that of *Ledésert et al.* [1993] and *Gertsch* [1995] at a decimetric scale in the laboratory. Only *Gertsch*

<sup>1</sup>Laboratoire de Combustion et de Détonique, Poitiers, France.

<sup>2</sup>Institut de Physique du Globe de Paris, Paris, France.

<sup>3</sup>Institutt for Energiteknikk, Kjeller, Norway.

<sup>4</sup>Laboratoire de Géologie Dynamique, Villeneuve d'Ascq, France.

Copyright 2000 by the American Geophysical Union.

Paper number 2000JB900149.  
0148-0227/00/2000JB900149\$09.00

[1995] actually reconstructed a three-dimensional fracture network from serial sections data, although he did not proceed beyond a 3-D visualization of the network.

In this paper, the geometry of a natural fracture network is fully characterized from the experimental serial sections obtained by *Ledésert et al.* [1993]. Our purpose is to reconstruct the fracture network in three dimensions, with a threefold objective. First, 3-D visualizations provide more direct insight into the network structure. Second, an appropriate 3-D description allows one to determine geometrical parameters that are not accessible in 2-D sections. Finally, it can also be used to investigate the transport properties of the network.

This paper is organized as follows. Some necessary concepts and terminology are introduced in section 2, where general results from previous numerical investigations of the geometrical and transport properties of random fracture networks are briefly recalled. The rock sample and the primary data acquisition are described in section 3. Section 4 is devoted to the 3-D reconstruction of the fracture network from the serial 2-D trace maps, which is performed by triangulating the fracture surfaces. The geometrical and topological properties of the network are addressed in section 5. Extensive results are provided, with emphasis on the connectivity. Finally, fluid flow and solute transport through the network are considered in sections 6 and 7 by solving the local transport equations in the fractures.

## 2. General Concepts and Terminology

The geometrical and topological properties of random fracture networks were systematically investigated by direct 3-D numerical simulations by *Huseby et al.* [1997]. Their transport properties were studied by *Koudina et al.* [1998] and *Huseby et al.* [1997] for fluid flow and solute transport, respectively. The most salient results of these works are summarized by *Adler and Thovert* [1999], who also provide an extensive survey of the related literature.

The results of the present work will be compared with the general results of these studies, and their numerical tools are used to investigate the transport properties of the real fracture network. Therefore some terminology and necessary concepts are introduced in this section.

### 2.1. Topology

The concept of excluded volume was introduced by *Balberg et al.* [1984] and it was extensively used in the context of continuum percolation. If a population of objects is uniformly distributed in space, the excluded volume  $V_{ex}$  is defined as the volume surrounding an object in which the center of another object must be in order for them to intersect. For example, consider monodisperse spheres with volume  $V_s$ ; it is obvious that two spheres intersect when the distance between their centers is less than one diameter; hence the excluded volume of a sphere is simply in terms of  $V_s$ ,

$$V_{ex} = 8 V_s, \quad (1)$$

for spheres. Let us now consider a set of randomly oriented convex polygons with perimeter  $P_p$  and area  $A_p$ ; each polygon is a 2-D object; the volume  $V_{ex}$  which surrounds a given polygon in which the center of another polygon must be in order for the two polygons to intersect is given by *Adler and Thovert* [1999]:

$$V_{ex} = \frac{1}{2} P_p A_p. \quad (2)$$

For anisotropic orientation distributions, different values of  $V_{ex}$  are obtained by a proper statistical averaging. It should be emphasized, however, that the definition of the excluded volume is meaningful only if the object locations are uniformly distributed in space.

Now suppose that the number of objects per unit volume, i.e., the volumetric density, is denoted by  $\rho$ . It is natural to use  $V_{ex}$  as a reference volume, and we may define the dimensionless density  $\rho'$  as the number of objects per volume  $V_{ex}$ :

$$\rho' = \rho V_{ex}. \quad (3)$$

In addition, from the definition of  $V_{ex}$ ,  $\rho'$  is also the average number of intersections per object if they are randomly located according to a Poisson process. Therefore, given the shape of the object and its orientation distribution (and thus  $V_{ex}$ ), definition (3) incorporates both volumetric and topological aspects.

The real network considered in this paper does not belong to the general class investigated by *Huseby et al.* [1997], since the fractures are not plane nor isotropically oriented, and possibly not uniformly distributed in space. Furthermore, the fracture sizes and shapes are very dispersed. Thus the density  $\rho$  should be expressed as a function of the fracture orientation, size, and shape, and  $V_{ex}$  should be obtained by a complex averaging procedure. The number of fractures in the network is too limited and the truncations by the sample boundaries too frequent to allow an accurate estimation of these quantities. However, the number of intersections per fracture directly provides an estimate of  $\rho'$ . Hence the topological properties of the real network can be compared with theoretical and numerical predictions for isotropic networks with the same connectivity.

The reduced density  $\rho'$ , based on the excluded volume, proved very successful for unifying the description of random isotropic networks of plane fractures. *Huseby et al.* [1997] showed that a percolation threshold takes place for  $\rho'_c = 2.26 \pm 0.04$  and that many topological properties such as the cyclomatic number or the density of finite blocks are functions of  $\rho'$  only.

A connected component of a fracture network is a set of fractures which are connected one to another. The number of such connected components for a network is denoted by  $\beta_0$ .

This definition is necessary for the introduction of the first Betti number, also called the cyclomatic number or genus, which is the number of independent cycles in the network [*Barret and Yust*, 1970]; it may be expressed as

$$\beta_1 = N_I - N_f + \beta_0, \quad (4)$$

where  $N_f$  and  $N_I$  are the numbers of fractures and fracture intersections, respectively.

An intrinsic volumetric cyclomatic number,  $\overline{\beta}_1$ , and the corresponding number of cycles per volume  $V_{ex}$ ,  $\beta'_1$ , are defined by

$$\overline{\beta}_1 = \frac{\beta_1}{V} \quad \beta'_1 = \overline{\beta}_1 V_{ex}. \quad (5)$$

By definition, the number  $\beta_0$  of connected components is small compared to  $N_f$  in well-connected networks; hence  $\beta_0$  can be neglected in (4), and one obtains

$$\overline{\beta}_1 = \left(\frac{\rho'}{2} - 1\right) \rho \quad \beta'_1 = \left(\frac{\rho'}{2} - 1\right) \rho'. \quad (6)$$

In addition, *Huseby et al.* [1997] and *Adler and Thovert* [1999] showed that the density  $\rho'_b$  of closed blocks can be fitted by a power law of  $\rho'$ :

$$\rho'_b = 5.7 \cdot 10^{-5} \rho'^{4.46}. \quad (7)$$

Finally, let us introduce the following notations. The area of fracture  $i$  is denoted as  $A_i$ ,  $i = 1, \dots, N_f$ . Its number of intersections with other fractures is  $n_i$ , with  $\sum_i n_i = 2N_I$ , since each intersection involves two fractures. The length of the intersection line of fractures  $i$  and  $j$ , if any, is denoted as  $l_{ij}$ ; the total intersection length for fracture  $i$  is  $L_i = \sum_j l_{ij}$ .

## 2.2. Flow

The following applies equally well to electrical conduction and fluid permeability. Since applications deal mainly with permeability, the flow language was preferred.

The solid matrix containing the fractures is assumed to be impervious. The flow of a Newtonian fluid at low Reynolds number is governed by the Stokes equations within a fracture, i.e., at a local scale characterized by a typical aperture  $b_0$ , which is assumed to be much smaller than the typical lateral extent  $D_0$  of the fracture. Because of the classical Poiseuille law the typical permeability  $\sigma_0$  of a fracture is expected to be of the order of

$$\sigma_0 = \frac{b_0^3}{12}. \quad (8)$$

At a scale  $\mathcal{L}'$ , which is intermediate between  $b_0$  and  $D_0$ , the flow is governed by the Darcy equation

$$\mathbf{j}' = -\frac{1}{\mu} \boldsymbol{\sigma}' \cdot \nabla p', \quad (9)$$

where  $\mathbf{j}'$  and  $\nabla p'$  are the locally averaged flow rate per unit width [ $L^2 T^{-1}$ ] and pressure gradient and  $\boldsymbol{\sigma}'$  [ $L^3$ ] is the fracture permeability tensor; dimensional quantities are indicated by a prime. The mass conservation equation becomes

$$\nabla'_S \cdot \mathbf{j}' = 0. \quad (10)$$

where  $\nabla'_S$  is the 2-D gradient operator in the mean fracture plane. The dependence of  $\boldsymbol{\sigma}'$  on the fracture characteristics was studied by *Mourzenko et al.* [1995, and references therein].

Note that if electrical conductivity is addressed, the shape of (9) and (10) remains the same;  $p'$  should be replaced by the electric potential  $\psi'$ ;  $\boldsymbol{\sigma}'$  would be the fracture conductivity tensor. These equations must be supplemented with no-flux conditions at the fracture edges and conservation (for the flux) and continuity (for pressure) equations along the fracture intersections.

Any standard overall boundary condition can be applied to the network. For instance, pressures or fluxes could be applied along inlet and outlet lines drawn on fractures of the network. In the particular case where the fracture networks are statistically homogeneous at the field scale, which is assumed to be large with respect to the lateral dimensions  $D_0$  of the fractures, a macroscopic pressure gradient  $\overline{\nabla p}$  induces an average flux  $\overline{\mathbf{v}}'_n$ , which is related to the pressure gradient by Darcy's law recalled by *Adler* [1992],

$$\overline{\mathbf{v}}'_n = -\frac{1}{\mu} \mathbf{K}'_n \cdot \overline{\nabla p}. \quad (11)$$

$\mathbf{K}'_n$  is the network permeability tensor [ $L^2$ ]. For isotropic networks it is a spherical tensor

$$\mathbf{K}'_n = K'_n \mathbf{I}. \quad (12)$$

It is convenient to introduce a dimensionless permeability tensor  $\mathbf{K}_n$ ,

$$\mathbf{K}'_n = K_0 \mathbf{K}_n \quad K_0 = \frac{\sigma_0}{R}, \quad (13)$$

where  $R$  is a typical lateral size of the fractures.

*Koudina et al.* [1998] developed general numerical tools to solve the local flow equations in fracture networks described by a 3-D triangular mesh, and they systematically investigated the flow properties of the same class of random networks of plane fractures as *Huseby et al.* [1997]. They showed that the permeability varies as

$$K_n = 0.0455 (\rho' - \rho'_c)^{1.57} \quad (3.5 \leq \rho' \leq 20). \quad (14)$$

*Snow* [1969] considered networks where all the fractures are infinite plane channels with an arbitrary orientation distribution. This is equivalent to assuming that the whole surface of all the fractures in the network may contribute to the flow and can be valid only in the limit of very dense networks.

For an isotropic network the permeability tensor is given by

$$\mathbf{K}'_{S_n} = \frac{2}{3} \sigma' \mathcal{S} \mathbf{I}, \quad (15)$$

where  $\mathcal{S}$  is the volumetric surface area of fractures. This result is easily generalized for anisotropic networks by introducing the fracture orientation distribution, which yields a nonspherical tensor  $\mathbf{K}'_{S_n}$ :

$$\mathbf{K}'_{S_n} = \int \int_{\Omega} \sigma'(\mathbf{n}) \mathcal{S}(\mathbf{n}) (\mathbf{I} - \mathbf{nn}) d^2\mathbf{n}, \quad (16)$$

where  $\Omega$  is the unit sphere and  $\mathcal{S}(\mathbf{n})d^2\mathbf{n}$  is the volumetric surface area of fractures with normal vector in the solid angle  $d^2\mathbf{n}$  around  $\mathbf{n}$ , with permeability  $\sigma'(\mathbf{n})$ .

For finite polygons,  $\mathcal{S}$  can be expressed in terms of the surface  $A_p$  and perimeter  $P_p$  of the polygons. Hence the dimensionless permeability in Snow's [1969] model network with the same surface density is

$$K'_{S_n}{}^{iso} = \frac{4}{3} \frac{R}{P_p} \rho', \quad (17)$$

where  $R/P_p$  is a shape factor, equal, for instance, to  $\sqrt{2}/8$ ,  $1/6$ , and  $1/2\pi$  for square, hexagonal, and circular fractures, respectively. The numerical calculations of Koudina *et al.* [1998] showed that (17) is indeed a possible asymptote for networks of finite fractures with very large densities.

### 2.3. Solute Transport

**2.3.1. Physical description.** Most of the understanding of solute transport phenomena in rock and soils has been gained in the context of porous media. Surprisingly, few contributions discuss the important case of fracture network transports, although fractures are likely to dominate transport if they are present in otherwise porous media. If the porosity is small, as in igneous rocks, or if the pore space is disconnected, as in chalk reservoirs, transport processes may completely depend upon the presence of a connected fracture network.

Consider a solute which is released in a (possibly curvilinear) surface embedded in a 3-D space, and define a surface concentration  $C'(\mathbf{r}', t')$ . The concentration evolves in time and space according to a convection-dispersion equation

$$\frac{\partial C'}{\partial t'} + \mathbf{v}' \cdot \nabla'_S C' - \nabla'_S \cdot (\mathbf{D}' \cdot \nabla'_S C') = \delta(\mathbf{r}' - \mathbf{r}'_0) \delta(t' - t'_0), \quad (18)$$

where  $\mathbf{v}'$  is the velocity of the convecting fluid,  $\mathbf{r}'$  is the solute position at time  $t'$ , and the Dirac distributions describe the initial source term, when the solute is released at location  $\mathbf{r}'_0$ , at time  $t'_0$ ;  $\mathbf{D}'$  is the local dispersion tensor. This dispersion tensor should be viewed as the average quantity obtained in the first upscaling from the microscopic molecular level. The dispersion tensor  $\mathbf{D}'$  is therefore a function of the microscopic fracture geometry and of the interstitial fluid velocity  $v_m$ , as well as of the molecular diffusivity  $d_m$ , and this function is assumed to be known.

The macroscopic Péclet number  $Pe_n$  can be defined as

$$Pe_n = \frac{\bar{v}'_n R}{d_m}, \quad (19)$$

where  $\bar{v}'_n$  is the magnitude of the average interstitial velocity  $\bar{\mathbf{v}}'_n$ , which can be expressed as

$$\bar{\mathbf{v}}'_n = \frac{V}{b_0 S} \bar{\mathbf{v}}'_n = \frac{1}{b_0 S} \sum_{i=1}^{N_t} \mathbf{j}'_i S_i, \quad S = \sum_{i=1}^{N_t} S_i, \quad (20)$$

where  $\mathbf{j}'_i$  is the flow rate in each triangle  $i$  with area  $S_i$ .

A particularly simple value of  $\mathbf{D}'$  is obtained when the local Péclet number  $Pe_i = \mathbf{j}'_i/d_m$  is small enough, since then  $\mathbf{D}'$  reduces to the molecular diffusion coefficient. The computations in the following were run in this simple case. Hence the results apply as long as the macroscopic Péclet number  $Pe_n$  does not exceed the ratio  $R/b_0$ .

Dimensionless quantities (without primes) may be introduced by

$$\mathbf{r}' = R \mathbf{r}, \quad \mathbf{v}' = \frac{d_m}{R} \mathbf{v}, \quad \mathbf{D}' = d_m \mathbf{D}, \quad t' = \frac{R^2}{d_m} t \quad (21)$$

With these notations, the dimensionless velocity  $\bar{\mathbf{v}}'_n$  is simply equal to  $Pe_n$ .

**2.3.2. Numerical simulation by the random walk method.** The random walk method, which does not require the assumption of spatially periodic medium, is well suited to study dispersion in the natural network considered here (cf. O. Huseby *et al.*, manuscript in preparation, 2000). The random walk algorithm can be described in the few following steps [Sallés *et al.*, 1993]. Release a large number  $N_p$  of particles numbered by the index  $i$  ( $i = 1, 2, \dots, N_p$ ), at locations  $\mathbf{r}_i(t_0)$ . In the following simulations it was convenient to release the particles in some inlet triangles; alternatively, they may all be released in one point.

Convect and diffuse each particle in time steps  $\delta t$ . The location at time  $t + \delta t$  is given as

$$\mathbf{r}_i(t + \delta t) = \mathbf{r}_i(t) + \mathbf{v}(\mathbf{r}_i) \delta t + \delta_{\mathcal{D}} \quad (22)$$

where  $\mathbf{r}_i(t)$  is the location at time  $t$ ,  $\mathbf{v}(\mathbf{r}_i)$  the velocity at location  $\mathbf{r}_i(t)$ , and  $\delta_{\mathcal{D}}$  a random diffusive step, whose magnitude is deduced from the local dispersion tensor, with a random direction.

The velocity field used in the random walk algorithm is uniform inside each triangle. When a triangle edge is encountered, the movement is continued with the same velocity, except if the triangle edge coincides with a fracture edge or an intersection. It is therefore important that each step is not too large compared to the triangle sizes.

When a particle encounters a fracture edge, it stops and the elapsed time to arrive at the edge is recorded. The remaining time is used in the subsequent step. Hence all the particles are kept at the same times, which is required for the calculation of the moments.

The fracture intersections are handled like the fracture edges. If a particle reaches a fracture intersection, it stops and the remaining time is again recorded and used in the subsequent step. From an intersection the particle may enter any of the four adjacent triangles, chosen at random with equal probabilities  $1/4$ . A new directed step is calculated from the velocity in the chosen triangle and a random diffusive displacement; this

new step may point into or out of the triangle; if it points out of the triangle, the particle did not leave the intersection and the procedure is resumed until the particle stays in the chosen triangle. This procedure yields the same results as the perfect mixing model, i.e., solute fluxes proportional to the outgoing fluid flow rates. Other mixing rules were investigated by O. Huseby et al. (manuscript in preparation, 2000).

The dispersion of the solute can be evaluated either by investigating the spatial distribution of particle locations  $\mathbf{r}_i$  at fixed times  $t$  or by investigating the distribution of times  $t_i$  used to travel a fixed distance  $\mathbf{r}$ .

In the first approach, the global moments of the spatial distribution of particles can be determined by the summation

$$\mathbf{M}_m = \frac{1}{N_p} \sum_{i=1}^{N_p} [\mathbf{r}_i(t) - \mathbf{r}_i(t_0)]^m, \quad (23)$$

After long times, the three first moments of the particle distribution in space converge to

$$M_0 = \text{const}, \quad (24a)$$

$$\mathbf{M}_1 = \bar{\mathbf{v}}^* t, \quad (24b)$$

$$\mathbf{M}_2 = \mathbf{M}_1 \mathbf{M}_1 + 2\mathbf{D}^* t, \quad (24c)$$

The dispersion tensor can be evaluated from  $\mathbf{M}_1$  and  $\mathbf{M}_2$  as

$$\mathbf{D}^* = \frac{1}{2} \frac{d}{dt} (\mathbf{M}_2 - \mathbf{M}_1 \mathbf{M}_1). \quad (25)$$

In the second approach, the global moments  $T_m$  of the travel time distribution for fixed displacements  $\mathbf{r}$  can be determined by the summation

$$T_m = \frac{1}{N_p} \sum_{i=1}^{N_p} (t_i - t_0)^m. \quad (26)$$

In this case, we have [Sahimi et al., 1986]

$$T_0 = \text{const}, \quad (27a)$$

$$T_1 = \frac{r_\xi}{\bar{v}_\xi^*}, \quad (27b)$$

$$T_2 = T_1^2 \left(1 + \frac{2D_\xi^*}{r_\xi \bar{v}_\xi^*}\right), \quad (27c)$$

where  $\xi$  is the direction of the applied pressure gradient.

If the dispersion is diffusive, that is, if both the spatial particle distribution at fixed times and the travel time distribution at fixed locations are Gaussian, both approaches yield the same dispersion coefficient. However, as we shall see in section 7.2, the dispersion process in the natural network is non-Gaussian, at least over the limited investigated spatial domain. Therefore the dispersion coefficient was determined both from (27b) and (27c) and from the following definition based on the spatial spread [Sahimi et al., 1986]:

$$\mathbf{D}^* = \left\langle \frac{(\mathbf{r} - \bar{\mathbf{v}}^* t_i)(\mathbf{r} - \bar{\mathbf{v}}^* t_i)}{2t_i} \right\rangle, \quad \bar{\mathbf{v}}^* = \left\langle \frac{\mathbf{r}}{t_i} \right\rangle. \quad (28)$$

This expression is similar to (25), except that the in-

stantaneous centered second-moment  $\mathbf{M}_2 - \mathbf{M}_1 \mathbf{M}_1$  is replaced by the quadratic mean deviation of the particle positions from the expected displacement  $\bar{\mathbf{v}}^* t_i$ ; deduced from the mean solute velocity  $\bar{\mathbf{v}}^*$  and from the arrival time  $t_i$ . Note that the mean solute velocity  $\bar{\mathbf{v}}^*$  can differ from the mean fluid velocity  $\bar{\mathbf{v}}_n^*$ , as discussed in section 7.

### 3. Primary Data

The present study was conducted on a block of dark grey Hercynian granite from La Peyratte, Deux-Sèvres, France. It is fine-grained (1 to 2 mm long crystals) and is crosscut by numerous fractures and veins surrounded by discolored alteration halos. The primary acquisition was undertaken by Ledéseret et al. [1993]. The granite block (about  $52 \times 35 \times 36 \text{ cm}^3$ ) was sawed into 9 parallel plates, 4 cm in thickness. Trace maps were drawn from the nine sections by visual examination of the alteration zones due to the circulation of hydrothermal fluids (Figure 1). The fracture pattern appeared to be composed of two main families A and B, at about  $\pm 30^\circ$  inclination angle from the vertical axis in Figure 1. These two sets are associated with one horizontal fracture (fracture 16 in Figure 1).

The fracture traces in each section were labeled, and the traces of a same fracture in successive sections were given identical labels. The rock sample contained  $\sim 240$  fractures. About 150 of them could be seen in a single plane. Their trace lengths ranged between 1 and 12 cm. The other 90 fractures could be followed through at least two planes, with trace lengths between 2.5 and 47 cm. Only six fractures could be traced through the nine sections.

The total surface area of fractures was estimated to be  $2.6 \text{ m}^2$ , and the block volume was estimated to be  $0.066 \text{ m}^3$ . Ledéseret et al. [1993] also quantified the total volume of altered rock and performed a fractal analysis of the fracture pattern based on scan line surveys on the 2-D maps.

### 4. Three-Dimensional Reconstruction

The three-dimensional reconstruction was performed by triangulating the fracture surfaces. As shown in Figure 1, the fracture traces in each section are often curved, and the fracture are also often twisted between successive sections. This feature introduces technical difficulties, with the consequence that the numerical tools devised by Huseby et al. [1997] and Koudina et al. [1998] for networks of plane polygons are not directly applicable here.

The triangulation procedure comprises three main steps. In the first step, mesh points are distributed along each fracture trace. This operation is partly manual but is computer-aided. The human operator selects points on a digitized image of the trace map on a computer screen and indicates whether a point is a standard point, a trace termination, or a trace intersection. In the second step, each fracture is separately trian-

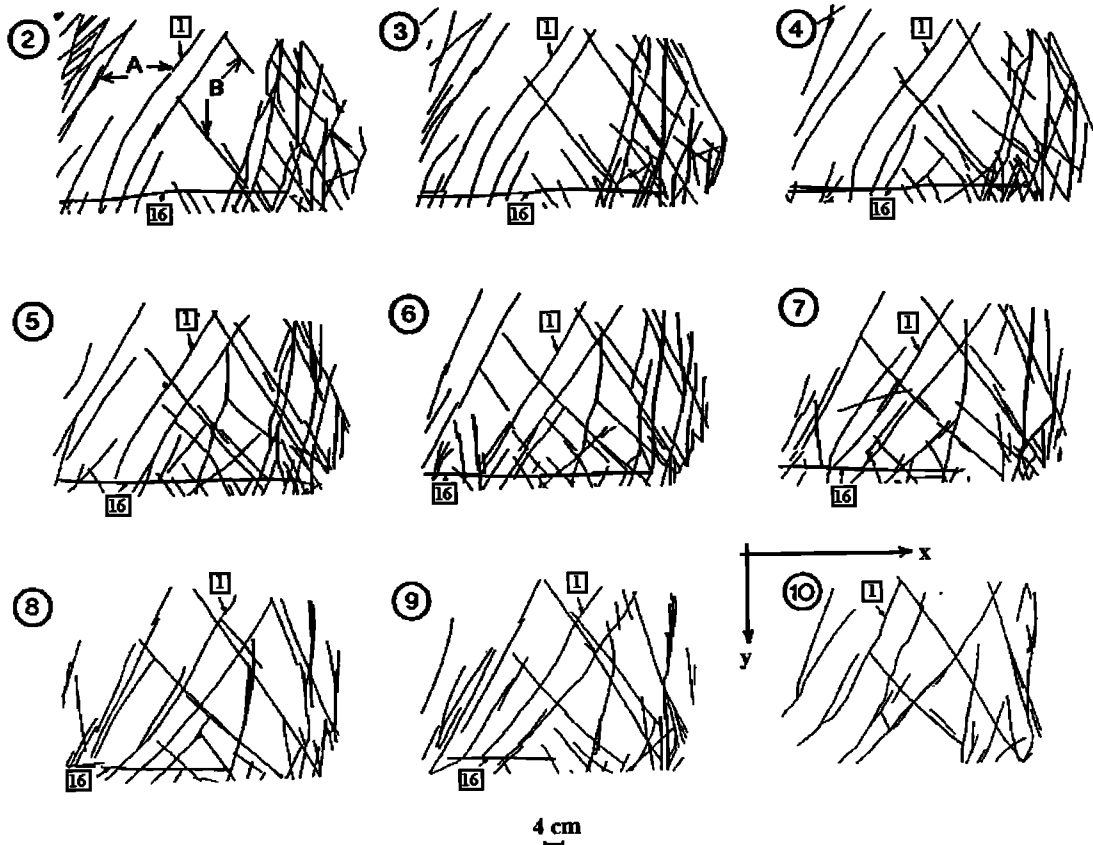


**Figure 1.** The nine successive trace maps. The traces of two fractures (1 and 16) are indicated in each section. Two fractures from families A and B are marked in the first section. (Reprinted with permission from *Ledésert et al.* [1993].)

gulated by joining the points that belong to its successive traces. For convenience, four artificial fractures are added to the network. Together with the upper and lower planes, they represent the outer surface of the rock sample. They are only intended to provide an easy way to introduce boundary conditions for the simulations of transport processes. These two conceptually simple steps are sufficient to allow 3-D visualizations of the network. *Gertsch* [1995] proceeded along these lines and stopped at this point.

Two potential biases should be mentioned here. First, the fractures are triangulated only between the observed traces, which is an approximation since there is no reason to assume that a fracture does not extend any further. Other rules were possible, such as prolongating the fracture halfway to the two surrounding planes; this would have raised the question as to the fracture trace length in these intermediate planes. These issues were ignored, because of lack of information and in order to keep things amenable.

The second bias could be more important. For the same reason as above, the 150 fractures that are visible in a single section were ignored in the triangulation. This may have two consequences. First, together with the first bias mentioned above, it leads to a lower density of fractures. This effect is probably not very serious since the total area of the triangulated fractures was

found equal to  $2.05 \text{ m}^2$ , as compared with the estimate  $2.6 \text{ m}^2$  of *Ledésert et al.* [1993], obtained by simply multiplying the total trace length by the section interspace divided by the dip angle cosine. The second effect might a priori be more significant. One may wonder whether these fractures yield a single trace because their orientations are close to the section direction. For instance, a third family of fractures could exist, approximately parallel to the planes of the trace maps, which would be overlooked in this data set. There are three reasons to explain why this possibility is unlikely. First, this third set would yield traces visible on the sides of the rock sample, which were not detected. Second, the typical size of the single traces is much smaller than the other traces ( $1 \sim 12 \text{ cm}$  versus  $2.5 \sim 47 \text{ cm}$ ); therefore these fractures probably yield a single trace simply because they are of lesser extension. Finally, the orientations of the fractures with two traces do not differ significantly from the orientations of the larger ones. Consequently, it is likely that the effect of these two approximations is to slightly underestimate the surface area of the large fractures and to filter out many small fractures, with a combined reduction in the total surface area of  $\sim 20\%$ , but without biasing the orientation distribution.

The third step in the triangulation is the derivation of the fracture intersections, and the combination of their 2-D triangulations around their intersection lines. It

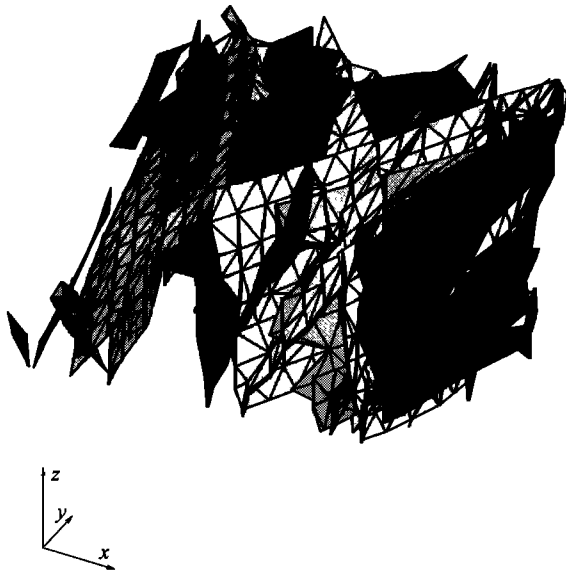


**Figure 2.** Visualization of the whole fracture network.

very often happens that three fractures intersect mutually; these situations are dealt with by considering fracture-pair intersections iteratively until all triangle intersections reduce to triangle edges or vertices.

Finally, the triangulation of the fracture network is cast into a list of  $\sim 3000$  mesh points defined by their coordinates and a list of  $\sim 9000$  triangles defined by their three vertices. The triangulated network is displayed in Figure 2. Fractures that do not intersect the side boundaries of the rock sample are called "internal" fractures. These fractures cannot be detected without actually dismantling the block, even though some of them are quite extensive.

## 5. Geometrical Characterization

A great deal of geometrical information can be obtained from the 3-D description of the network. Some is described in Figures 3 to 6.

The orientation distribution is characterized in Figure 3. The distributions of the normal vector to the triangles are given with or without weighting by the triangle areas. The mean overall orientations of the whole fractures are also given in Figure 3b. It was determined from the surface average of the normal vectors to the triangles in each fracture. These plots, which are based on the trace maps, are simply another representation of the data set presented in Figure 1. The two families *A* and *B* at  $\pm 30^\circ$  with respect to the *x* axis are clearly visible, as well as fracture 16, whose normal vector is perpendicular to the *x* axis. It is also apparent that all fractures are roughly parallel to the *z* axis, i.e., normal to the cross sections in Figure 1.

The histogram of the fracture surface areas  $A_i$ , displayed in Figure 4a, shows that 60% of the fractures have areas smaller than  $100 \text{ cm}^2$  and 85% smaller than  $400 \text{ cm}^2$ , whereas a few fractures have areas larger than  $1000 \text{ cm}^2$ , i.e., comparable with the cross section of the

whole sample. This dispersion is probably underestimated, since larger fractures are more likely to be cut by the sample boundaries and since the smallest fractures (which left a single trace in the serial sections) have been ignored. The same histogram restricted to the internal fractures (Figure 4b) does indeed show a larger proportion of very small fractures and a lesser proportion of large fractures. The cumulated distribution functions are compared in Figure 4c.

The histogram of the number  $n_i$  of intersections per fracture is shown in Figure 4d. The vast majority of fractures (84%) has 0 to 9 intersections with others. The remaining ones have 10 to 18 intersections, except for fracture 16 which crosses 36 fractures. Fractures of set *A* mainly cross fractures from set *B*, and vice versa. An interesting point here is the existence of a distribution with a relatively long tail.

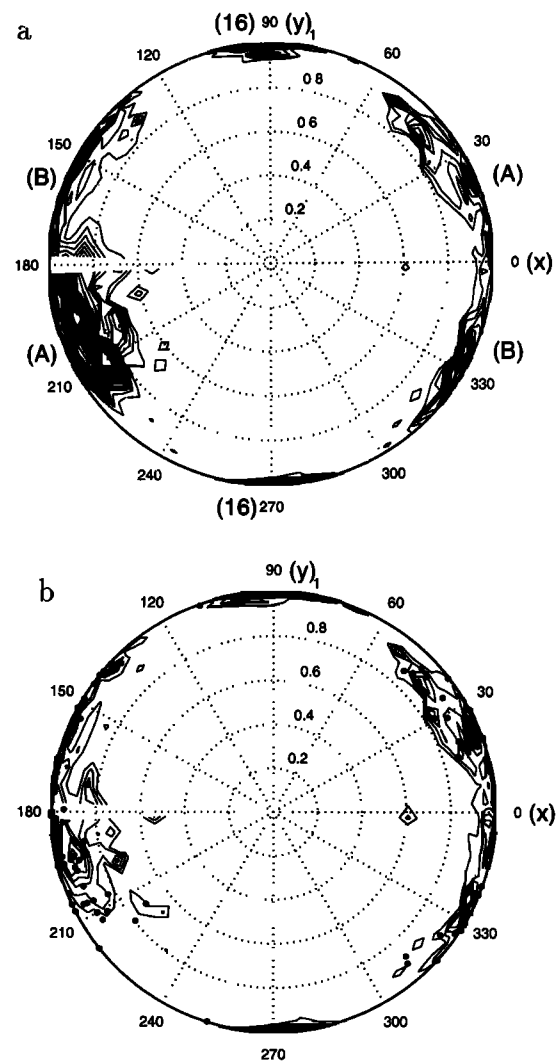


**Figure 3.** Distributions of the unit vectors normal to the triangles, (a) in numbers and (b) weighted by the areas, in projection onto the (*x*, *y*) plane. The origin of the azimuthal angle is aligned with the *x* axis. Families *A* and *B* and fracture 16 are marked in Figure 3a. The solid dots in Figure 3b correspond to the surface-averaged normal vectors of the whole fractures.

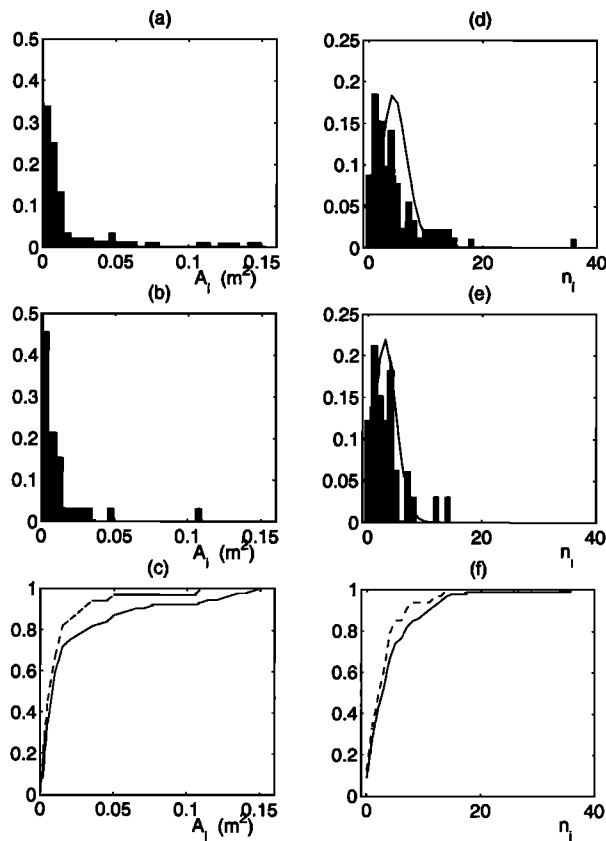


**Figure 4.** Histograms (a and b) of the fracture surface areas  $A_i$ , in  $m^2$  and (d and e) of the number  $n_i$  of intersections per fracture. Figures 4a and 4d are relative to all the fractures in the network, while the fractures which intersect the lateral boundaries of the sample are removed in Figures 4b and 4c. The solid line in (d,e) is the Poisson distribution with the same average. (c and f) The cumulated distribution functions corresponding to Figures 4a and 4b and to Figures 4d and 4e, respectively. The solid (dashed) line corresponds to the complete (filtered) network.

The average number of intersections per fracture is  $\rho' = 4.76$ , and the variance is equal to 26.6. Huseby *et al.* [1997] systematically investigated the topological properties of random networks of randomly oriented plane polygonal fractures and showed that a continuous path across these networks exists for  $\rho'$  greater than a percolation threshold  $\rho'_c \approx 2.3$ . Moreover, for  $\rho' \geq 4$ , more than 98% of the fractures are connected to the percolating cluster [Koudina *et al.*, 1998]. Hence the present network is fairly well connected, and indeed, only six fractures, out of a total number of 90, are not connected to the large cluster formed by the others. Hence the simple isotropic model provides reasonable orders of magnitude.

As a comparison, the Poisson distribution with the same average, which is expected if the fractures are randomly located and if the truncation effects are ignored, is also plotted in Figure 4d and obviously deviates from the data. Figure 4e is the counterpart of Figure 4d

for internal fractures. Although the average number of intersections per fracture is smaller,  $\rho' = 3.36$ , the two distributions are not dramatically different, as shown in Figure 4f.

The crack surface area and intersections can be obtained directly from the serial sections without any 3-D reconstruction. However, other geometrical terms such as the lengths  $l_{ij}$  of the fracture/fracture intersection lines can only be obtained from a 3-D description; they have been evaluated, and their histogram is plotted in Figure 5a. Their distribution is very broad. The value of  $l_{ij}$  ranges from  $\sim 2$  mm, which is close to the resolution of the data, to  $\sim 400$  mm, which is comparable with the overall sample size. The median value is  $\sim 100$  mm but obviously cannot be considered as a typical value of the intersection length. Therefore although each fracture crosses about five other fractures on average, which makes the network well connected from a topological point of view, these intersections may have very different weights for transport processes; indeed, only the long intersections will play an important role

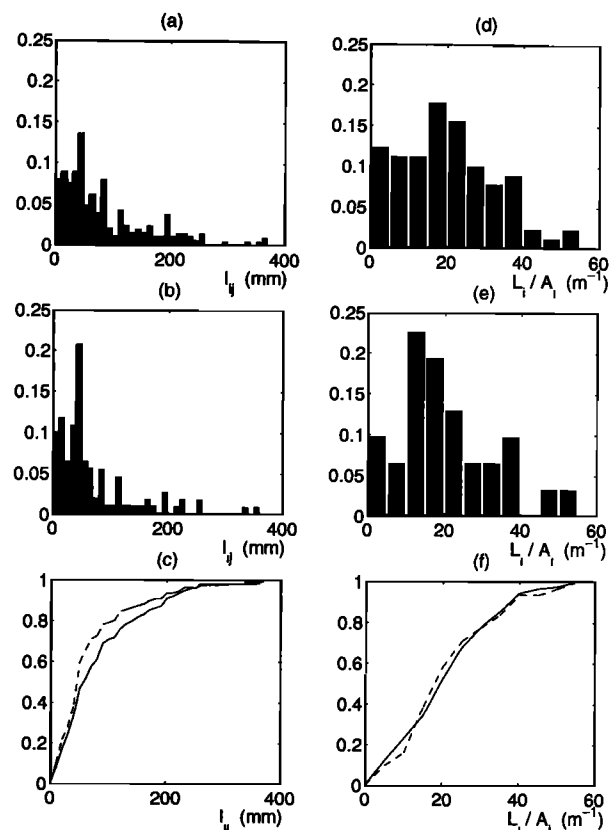


**Figure 5.** Histograms (a and b) of the intersection lengths  $l_{ij}$ , in millimeters and (d and e) of the total intersection length per fracture and per unit area  $L_i/A_i$ , in  $m/m^2$ . Figures 5a and 5d are relative to all the fractures in the network, while the fractures which intersect the lateral boundaries of the sample are removed in Figures 5b and 5e. (c and f) The cumulated distribution functions corresponding to Figures 5a and 5b and to Figures 5d and 5e, respectively. The solid (dashed) line corresponds to the complete (filtered) network.

in these processes, while the short ones will probably play a minor role. This last comment only applies to well-connected networks such as the one presented here; for networks close to the percolation threshold these short intersections could still be crucial for transport processes.

Again, the same statistics for the internal fractures are presented in Figure 5b and compared to the whole network in Figure 5c. Although the overall range of intersection lengths are identical, shorter intersections are observed, on average, in the internal fractures, probably because of their smaller size. This is confirmed by the histogram of the total intersection length per fracture and per unit area  $L_i/A_i$  shown in Figure 5d. For most fractures (94%),  $L_i/A_i$  ranges between 0 and 40  $m^{-1}$ , and for a few it reaches 55  $m^{-1}$ . The distribution is still broad, considering that it is normalized by the fracture areas, but less than the individual intersection lengths in Figure 5a; the distribution is remarkably uniform between 0 and 40 mm. Thus it is reasonable to define a typical areal density of intersection, roughly equal to 20  $m^{-1}$  ( $\pm 100\%$ ). The results in Figure 5d are not subject to truncation bias, since truncation by the sample boundaries simultaneously affect the apparent fracture area  $A_i$  and the total intersection length  $L_i$ . Indeed, the same histogram evaluated over the internal fractures (Figure 5e) is very similar to the previous one, as shown by the comparison of the cumulated distribution functions in Figure 5f. The same comments as before could be made about the consequences on transport properties.

The finite block identification algorithm described by Huseby *et al.* [1997] has been run on this data set. It is obviously not devoid of a truncation bias, since most fractures intercept the sample boundaries. A single finite block was found (Figure 6), with a volume 33.8

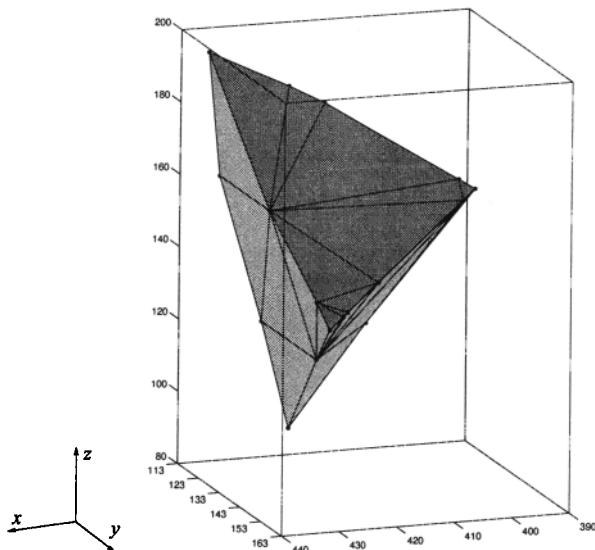


**Figure 6.** Finite block bounded by the four fractures 16, 18, 20, and 39. Graduations are in millimeters, and the block volume is 33.8  $cm^3$ .

$cm^3$ . This small number of blocks is not surprising considering that the network is made up of the fracture sets *A* and *B* and of fracture 16, which tessellate the space into prismatic columns with axes normal to the planes of Figure 1. Fractures parallel to these planes are lacking, and so these columns are not partitioned into finite blocks.

These observations can be compared with the theoretical and numerical results presented in section 2.1. In the following, superscripts *mes* and *iso* refer to the measurements and to the results (equations (6) and (7)) for isotropic networks, respectively. The volumetric fracture density was deduced from the number  $N_f=90$  of fractures and the sample volume  $V=0.066 m^3$ :

$$\rho = \frac{N_f}{V} = 1364 m^{-3}. \quad (29)$$

The reduced density  $\rho'$  can be obtained from the total number of intersections  $N_I=214$ :

$$\rho' = \frac{2N_I}{N_f} = 4.76. \quad (30)$$

Using (29), (30), and (3), an apparent mean excluded volume is evaluated as

$$V_{ex} = \frac{\rho'}{\rho} = 3.49 \times 10^{-3} m^{-3}. \quad (31)$$

Since six fractures are isolated and all others form a single connected cluster,  $\beta_0=7$ . The total cyclomatic number is obtained from (4):

$$\beta_1^{mes} = N_I - N_f + \beta_0 = 131. \quad (32)$$

Hence the volumetric cyclomatic numbers  $\bar{\beta}_1$  and  $\beta_1'$  are

$$\bar{\beta}_1^{mes} = \frac{\beta_1^{mes}}{V} = 1985 m^{-3}, \quad \beta_1'^{mes} = \bar{\beta}_1^{mes} V_{ex} = 6.93. \quad (33a)$$

These results compare well to the prediction from equation (6)

$$\bar{\beta}_1^{iso} = 1882 m^{-3}, \quad \beta_1'^{iso} = 6.57. \quad (33b)$$

Note that the fit (7) for isotropic random networks yields  $\rho_b^{iso} = 0.0603$ , i.e.,  $N_b^{iso}=1.14$ , in excellent agreement with the experimental value.

Note finally that  $\rho'$  was determined here by actually measuring the number of intersections per fracture, which is possible only when a 3-D reconstruction of the network is performed. As a comparison, suppose that one attempts to obtain this number by assuming that the fractures are randomly oriented disks with radius  $R$ . Then the total fracture area  $S=2.05 m^2$  is equal to  $N_f \pi R^2$ ;  $R$  is equal to 0.085 m, the corresponding excluded volume is  $V_{ex} = \pi^2 R^3 = 6.09 \cdot 10^{-3} m^3$  (see equation (2)), and  $\rho' = N_f V_{ex}/V=8.3$ . Hence the simple isotropic model provides a correct order of magnitude for  $\rho'$ . It overestimates it only by a factor 2, which is quite remarkable in view of the fact that the real network is mostly composed by two families of fractures as shown in Figure 3.

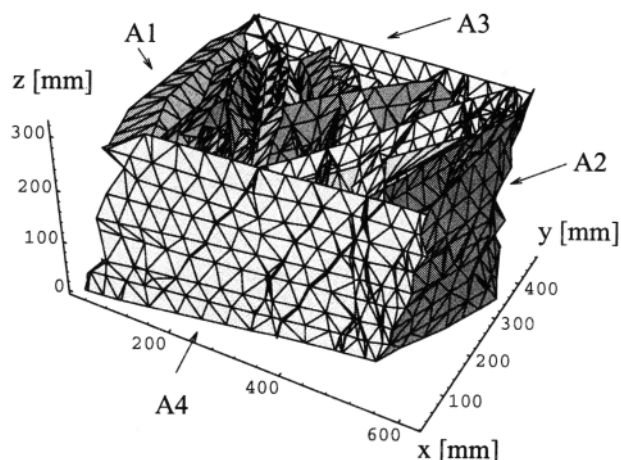


**Figure 7.** Artificial fractures A1-A4 which surround the sample volume, used to impose the hydraulic boundary conditions. Graduations are in millimeters.

## 6. Flow Properties

The numerical tools of *Koudina et al.* [1998] were applied to study the flow properties of the natural fracture network. The triangulation described in section 4 is used to define the mesh of the finite volume method for the numerical solution of the flow equations.

As already mentioned, four artificial fractures, A1-A4, were added to the network, to facilitate the application of hydraulic boundary conditions. They are oriented roughly normal to the  $x$  and  $y$  axes; together with the upper and lower sections, they entirely surround the sample volume (see Figure 7). They contain all the intersection lines of the fractures with the sample boundaries. The permeability of the artificial fractures is set to zero.

The boundary conditions were chosen in the simplest possible way. Suppose that a pressure gradient is imposed along the  $x$  direction; constant pressures are imposed on the two opposite faces normal to this direction. No additional lateral boundary condition is imposed along the  $y$  and  $z$  axes, except for the standard no flux condition along the fracture edges.

Because of the lateral boundary conditions the permeability tensor obtained by solving the mass conservation equation (10) is reduced to its diagonal terms.

In the absence of any information the fractures were arbitrarily given a constant and uniform permeability  $\sigma_0$ , which can be related to the constant aperture  $b_0$  by (8). The permeability scale  $K_0$  is given by (13), where the length scale  $R$  is equal to 100 mm.

The network permeability can also be evaluated by means of *Snow's* [1969] model by adding the contribution of each triangle to the integral in (12). We denote by  $K_{nu}$  and  $K_{Sn}$  the dimensionless tensors derived from the numerical calculations and by *Snow's* model, respectively; they are equal to

$$K_{nu,xx} = 0.66 \quad K_{nu,yy} = 1.89 \quad K_{nu,zz} = 2.0 \quad (34a)$$

$$(\sigma' = \sigma_0)$$

$$K_{Sn,xx} = 1.15 \quad K_{Sn,yy} = 2.54 \quad K_{Sn,zz} = 2.8. \quad (34b)$$

Hence the exact numerical calculations show that permeability is much larger along the  $y$  and  $z$  axes, which corresponds to the main orientation of the fractures as shown in Figures 2 and 3. *Snow's* model provides a correct order of magnitude for  $K_{nu}$ , but it smooths out the differences along the three axes. The prediction (14) which applies for isotropic networks of hexagonal fractures yields  $K_n \approx 0.18$ , which underestimates  $K_{nu}$  by a factor of about 10. Conversely, the values of  $K_{nu}$  in (34a) correspond in (14) to a density  $\rho' \approx 12$ . This probably results from a lower proportion of stagnant zones in the real network than in the random ones. The same reason explains the success of *Snow's* model.

For illustration, the computations have been repeated in a situation of weak disorder, where the local permeabilities  $\sigma'$  in the triangles are randomly and uniformly distributed between 0 and  $2\sigma_0$ , without any spatial correlation. Since the average  $\sigma'$  remains equal to  $\sigma_0$ , (12) still yields (34b). However, the full computation yields slightly lower permeabilities:

$$K_{nu,xx} = 0.59 \quad K_{nu,yy} = 1.66 \quad K_{nu,zz} = 1.9 \quad (34c)$$

$$(0 \leq \sigma' \leq 2\sigma_0).$$

Larger effects can be expected for broader permeability distributions, such as lognormal distributions.

The flow in a fracture that is present in the nine trace maps of Figure 1 is displayed in Figure 8. The flux

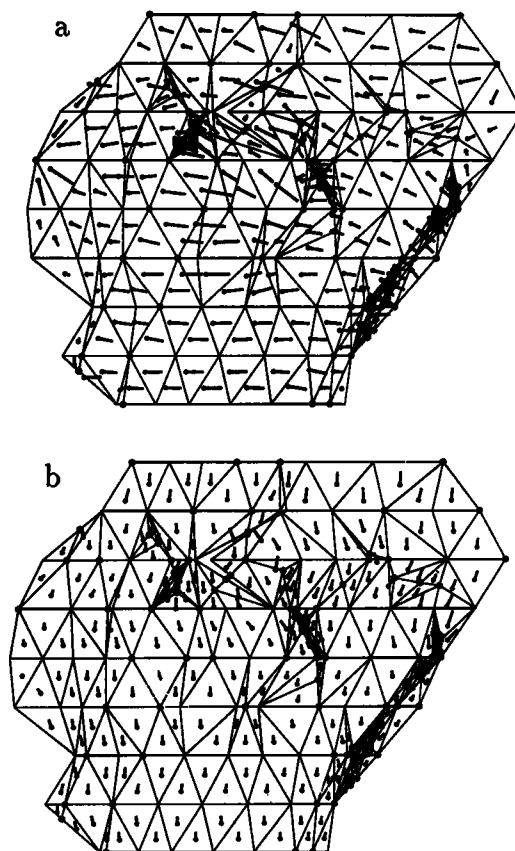


**Figure 8.** Fluxes in a fracture of the natural network. The pressure gradient is applied along (a) the  $y$  direction, and (b) the  $z$  direction.

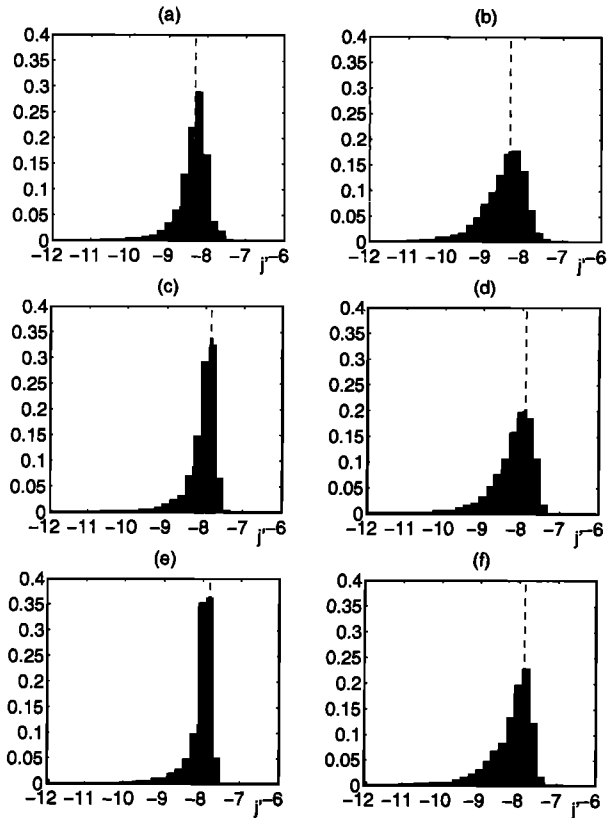


**Figure 9.** Histograms of the decimal logarithm of the flow rate  $j'$  in the triangles for a mean flow direction along the (a and b)  $x$  axis, (c and d)  $y$  axis, and (e and f)  $z$  axis. The histograms are weighted by the triangle areas. The local permeabilities are all equal to  $\sigma_0$  in Figures 9a, 9c, and 9e; they are uniformly distributed between 0 and  $2\sigma_0$  in Figures 9b, 9d, and 9f. The vertical dashed line is the surface average corresponding to the global flux.

discontinuities observed in Figure 8 correspond to the exchanges between fractures.

Finally, the histograms of the local flow rates  $j'$  in the triangles are given in Figure 9 for the three directions of the main flow and for the uniform and random permeability distributions corresponding to (34a) and (34c). The histograms are weighted by the triangle areas, but the histograms in numbers of triangles are very similar. The vertical dashed line corresponds to the mean flow rate in the fractures  $\bar{j}'$ , which yields the same global flux in an isotropic network of infinite plane fractures with the same fracture density. It appears that many local fluxes exceed  $\bar{j}'$  for the flow along the  $x$  direction. This stems from the fact that most fractures are very inclined with respect to the  $x$  axis (generally  $\pm 60^\circ$ ; see Figures 2 and 3); hence the projections of the local flux vectors onto the main flow direction are much smaller than their magnitude. In other words, the flow is very tortuous. This feature is much less pronounced for the flow along the  $z$  axis, since all the fractures are close to vertical. An intermediate situation is observed for the flow along the  $y$  axis, since the fractures lie at  $\pm 30^\circ$

from this direction. The flux distributions in Figures 9b, 9d, and 9f for random local permeabilities are significantly broader than those in Figures 9a, 9c, and 9e for uniform local permeabilities.

## 7. Solute Transport

### 7.1. Random Walk Simulations

The flow fields obtained in section 2.2 by imposing a pressure gradient successively along the  $x$ ,  $y$ , and  $z$  directions were used as input data for the random walk simulations. The four artificial fractures A1-A4 used to impose external pressure conditions (see Figure 7), were used again to define the boundary conditions for the dispersion problem. In  $x$  and  $y$  directions, inlet and outlet triangles are defined as triangles adjacent to the upstream and downstream surfaces with imposed pressures, respectively. In the  $z$  direction the upper and lower sections play the same role.

Dispersion was investigated in the three directions using  $N_p = 2000$  particles and six Péclet numbers  $Pe_n = 0.01, 0.1, 1.0, 10, 100$ , and  $1000$ . The initial positions of the  $N_p$  particles are uniformly distributed in the inlet triangles. The particles are then transported according to the random walk algorithm and the times  $t_i$  used by each particle  $i$  to travel three distances  $L_1$ ,  $L_2$ , and  $L_3$  are recorded. These distances were set equal to  $L_1=50$  mm and  $L_2=100$  mm in all directions and to  $L_3=340$  mm, 225 mm, and 240 mm in the  $x$ ,  $y$ , and  $z$  directions, respectively. The travel time distributions and equations (26)-(28) are used to estimate the longitudinal dispersion coefficients  $D^*(L_1)$ ,  $D^*(L_2)$ , and  $D^*(L_3)$  at  $L_1$ ,  $L_2$ , and  $L_3$ .

### 7.2. Results

The travel time distributions at  $L_1$ ,  $L_2$ , and  $L_3$  are given for  $Pe_n = 0.01, 10$ , and  $1000$  in Figure 10, for pressure gradients imposed in the  $x$ ,  $y$ , and  $z$  directions, respectively. The mean arrival time  $\langle t'_i \rangle$  can differ significantly from the expected value  $L/\bar{v}_n^*$  based on the fluid velocity. Along the  $x$  direction, the solute always moves slower than the convecting fluid, whereas it moves faster along the  $z$  direction. In the  $y$  direction the solute moves slightly faster than the fluid for  $Pe_n = 0.01$  and slower for  $Pe_n \geq 0.1$ .

These differences result in part from the injection conditions. The mean particle velocity is expected to be equal to the fluid velocity when the solute concentration is uniform, that is, when the sampling of the velocity field by the particles is equivalent to a volume averaging; this corresponds to injection rates at the upstream domain boundary proportional to the local incoming flux. The spatially uniform initial distribution adopted here corresponds to a different sampling of the velocity field, and different mean velocities can be obtained, depending on the details of the upstream flow conditions. Such differences should of course vanish over longer distances, when sensitivity to the injection conditions is damped out by the diffusive transverse mixing. Recall also that

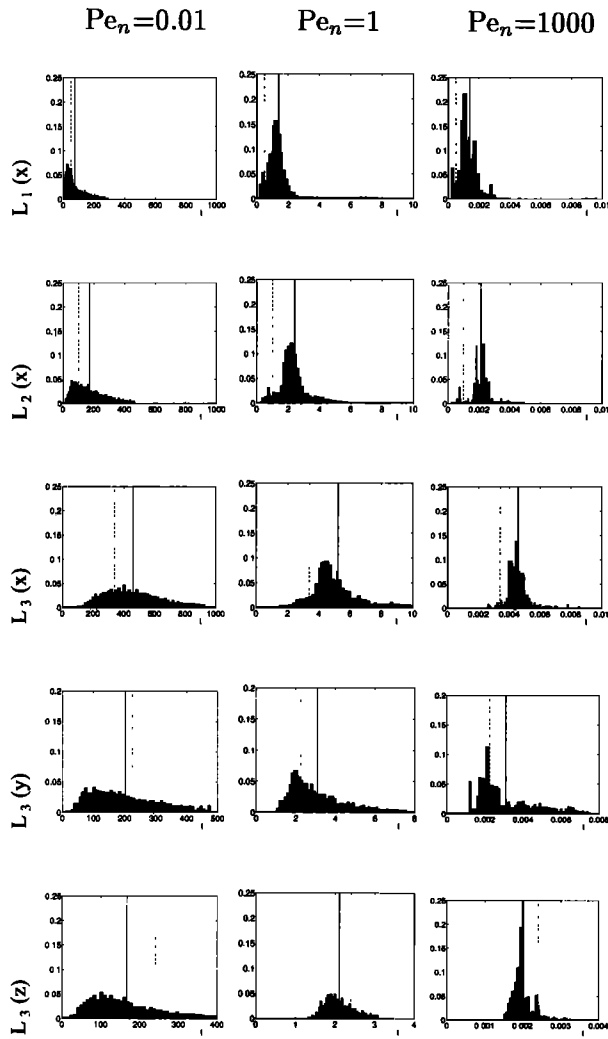


**Figure 10.** Histograms of the dimensionless arrival times  $t_i$  for a flow along the  $x$  direction at fixed distances  $L_1 = 50$  mm (first row),  $L_2 = 100$  mm (second row), and  $L_3 = 340$  mm (third row), and for flows along the  $y$  and  $z$  directions, at  $L_3 = 225$  mm (fourth row) and  $L_3 = 240$  mm (fifth row), respectively. The columns correspond to Péclet numbers  $Pe_n = 0.01, 1.0,$  and  $1000,$  respectively. The vertical lines are the mean arrival time  $\langle t_i \rangle$  (solid) and the arrival time expected from the fluid velocity  $L/R\bar{v}_n^*$  (dashed).

the random walk simulations were stopped once the particles reached the prescribed distance  $L$ , i.e., before they crossed the whole rock sample. Hence they do not experience all the velocities that are included in the volume average  $\bar{v}_n^*$ .

All the travel time distributions in Figure 10 are asymmetric, with long tails. Asymmetric, and therefore non-Gaussian, travel time distributions are frequently observed for dispersion processes in porous media [Sahimi, 1993, and references therein]. This can be explained by stagnant zones [Coats and Smith, 1964]; particles that are trapped in stagnant zones are retarded and have larger travel times compared to particles which escape trapping. If the sample is large compared to the

stagnant zones, all particles are exposed to trapping, and the stagnant zones yield a symmetric dispersive effect, unless the medium is inhomogeneous with respect to the distribution of stagnant zones. Conversely, if the sample is too short for all particles to experience trapping in stagnant zones, arrival times of trapped particles are large compared to travel times of the majority of particles, which yield asymmetric, long-tailed travel time distributions. A similar effect occurs for large, but heterogeneous samples; in this case, individual particles are exposed to stagnant zones depending on the path they follow through the medium.

The dispersion coefficients obtained from the spatial spread via equation (28), and from the temporal analysis in equation (27), are denoted by  $D_{||a}^*$  and  $D_{||t}^*$ , respectively. In addition, a dispersion coefficient  $D_{||s}^*$  has been directly estimated from equation (25), for a flow along the  $y$  direction, by recording the displacements  $L_i$  of the particles at a fixed time  $T$ , in order to evaluate the instantaneous moments  $M_1$  and  $M_2$ . The time  $T$  was set so that  $\bar{v}_n^* T = L_3/2$ .

The dispersion coefficients obtained from the three procedures, for various Péclet numbers, are compared in Figure 11. All the statistical procedures are seen to

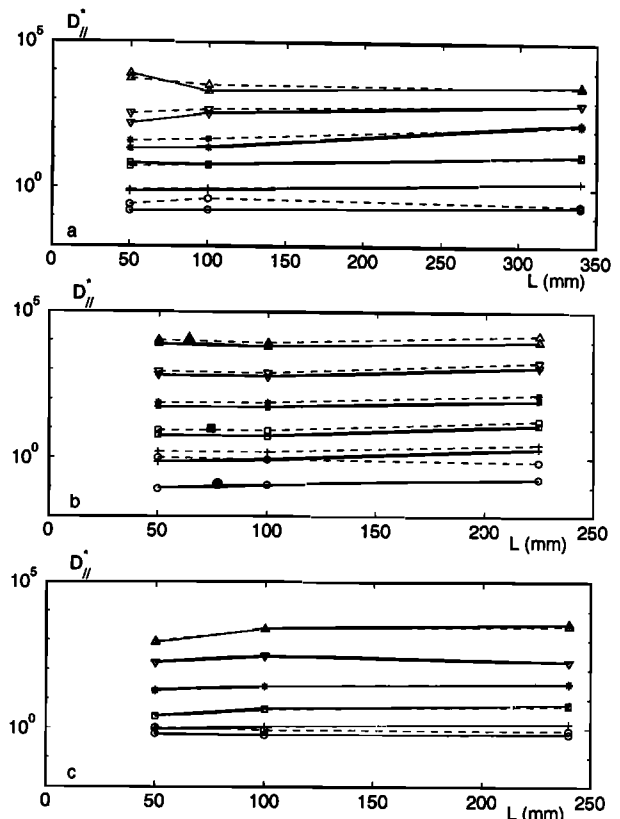


**Figure 11.** Dispersion coefficients  $D_{||t}^*$  (solid),  $D_{||a}^*$  (dashed) and  $D_{||s}^*$  (solid symbols) for a flow along the (a)  $x$ , (b)  $y$ , and (c)  $z$  directions versus the sampling distance from the inlet  $L$  (for  $D_{||t}^*$  and  $D_{||a}^*$ ) or the instantaneous mean displacement  $\langle L_i \rangle$  (for  $D_{||s}^*$ ). Data are for  $Pe_n = 0.01$  (circles),  $0.1$  (crosses),  $1$  (squares),  $10$  (stars),  $100$  (inverted triangles), and  $1000$  (triangles).

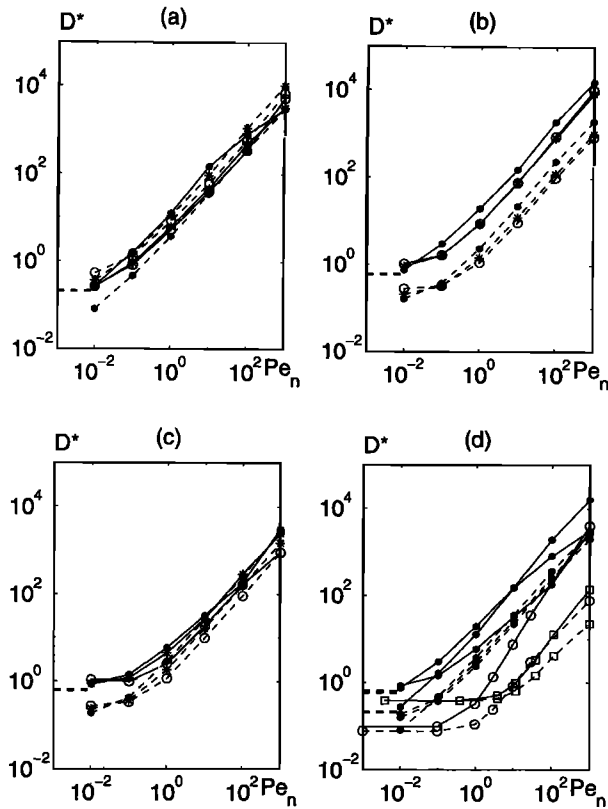


**Figure 12.** Dispersion  $D_{\parallel a}^*$  (solid lines) and  $D_{\perp a}^*$  (dashed lines) as functions of the Péclet number for a pressure direction along the (a)  $x$  direction, (b)  $y$  direction, and (c)  $z$  direction, measured at distances  $L_1$  (open circles),  $L_2$  (stars), and  $L_3$  (solid circles) from the inlet. The horizontal lines are the predictions of  $D_{\parallel}^*$  from equations (34a) and (35) for vanishing  $Pe_n$ . The results for  $L_3$  (solid circles) for the three flow directions are compared in Figure 12d to the data of O. Huseby et al. (manuscript in preparation, 2000) for isotropic networks of hexagonal fractures with density  $\rho' = 4$  (open circles) and 12 (squares).

yield consistent results, especially for  $Pe_n \geq 0.1$  and for the longest travel distances. Hence the non-Gaussian effects mentioned by Sahimi [1993] are very limited in the network studied here, and  $D_{\parallel a}^*$  is very close to  $D_{\parallel i}^*$ .

The dispersion coefficients  $D_{\parallel a}^*$  estimated at distances  $L_1$ ,  $L_2$ , and  $L_3$  for a flow along the  $x$ ,  $y$ , and  $z$  directions are plotted against the Péclet number in Figure 12. The transverse dispersion coefficient  $D_{\perp a}^*$  evaluated by the same method from the transverse displacements of the particles is also plotted in Figure 12.

The same behavior is observed in all cases; for small  $Pe_n$ ,  $D_{\parallel a}^*$  tends to a constant limit, and for large  $Pe_n$ ,  $D_{\parallel a}^*$  increases approximately as a power of  $Pe_n$ . The transition between the two regimes takes place in the range  $10^{-2} \leq Pe_n \leq 1$ .  $D_{\perp a}^*$  follows the same trends; it is generally smaller than  $D_{\parallel a}^*$ , except for the  $x$  direction, where the two dispersion coefficients are of the same magnitude.

In the limit  $Pe_n \rightarrow 0$ , where dispersion is reduced to diffusion, the dimensionless permeability and dispersion tensors are related by

$$D^* = \frac{V}{RS} K = \frac{b_0}{R\phi} K \quad (35)$$

where  $\phi = b_0 S/V = 0.032$  is the porosity. Recall that  $R=100 \text{ mm} = 100 b_0$ . The values of the longitudinal dispersion coefficient predicted by (35) in combination with (34a) are indicated by the horizontal lines in Figure 12. A good agreement is observed with the numerical data.

For large Péclet numbers,  $D_{\parallel a}^*$  seems to increase in Figure 12 as a power of  $Pe_n$ , for  $Pe_n \geq 10$ . A least squares fit of the data for  $Pe_n \geq 10$  yields

$$D_{\parallel a}^* = \kappa Pe_n^\alpha \quad (36)$$

with the prefactors  $\kappa$  and exponents  $\alpha$  given in Table 1. It is interesting to note the nearly linear behavior for  $Pe_n \geq 10$ , which should be compared to results in stochastic fracture networks obtained by O. Huseby et al. (manuscript in preparation, 2000), where dispersion for  $Pe_n \geq 100$  can be described by the power law (36), with an exponent  $\alpha$  which depends on the fracture density  $\rho'$ ;  $\alpha$  tends toward 2 close to the percolation threshold and toward 1 for dense networks. For the natural network considered here, the density was estimated in section 5 to  $\rho' = 4.76$ , which corresponds to a fairly well connected network.

For the isotropic networks of monodispersed hexagonal fractures considered by O. Huseby et al. (manuscript in preparation, 2000), the exponent  $\alpha$  was estimated to 1.3 for  $\rho' = 5.0$ , and to 1.1 for  $\rho' = 12.0$ . In view of the fact that the fractures in the natural network are by no means monodisperse hexagons, the exponents compare fairly well. Recall also that the results of O. Huseby et al. (manuscript in preparation, 2000) are relative to infinite periodic networks, in the long time limit, i.e., when dispersion has reached a Gaussian regime, whereas the present data correspond to short-time measurements.

**Table 1.** Exponent  $\alpha$ , Prefactor  $\kappa$ , and Regression Coefficient  $r$  of the Fits (36) of  $D_{\parallel a}^*$  versus  $Pe_n$  for  $Pe_n \geq 10$

$L$	$\alpha$	$\kappa$	$r$
<i>Case x</i>			
$L_1 = 50 \text{ mm}$	1.07	3.02	0.9979
$L_2 = 100 \text{ mm}$	0.93	5.99	0.9983
$L_3 = 340 \text{ mm}$	0.66	35.4	0.9979
<i>Case y</i>			
$L_1 = 50 \text{ mm}$	1.07	6.59	0.9999
$L_2 = 100 \text{ mm}$	1.02	7.59	0.9999
$L_3 = 225 \text{ mm}$	1.01	16.1	0.9986
<i>Case z</i>			
$L_1 = 50 \text{ mm}$	0.85	2.85	0.9974
$L_2 = 100 \text{ mm}$	0.98	2.96	0.9995
$L_3 = 240 \text{ mm}$	0.99	2.74	0.9904

A comparison with the data for networks of hexagonal fractures with densities  $\rho'=4$  and 12 is provided in Figure 12d. For small Péclet numbers the dispersion coefficients for  $\rho'=12$  are in better agreement with the computed values in the real network. This is a direct consequence of (35), since the permeability of the present network corresponds to that of isotropic networks of hexagons with  $\rho' \approx 12$  due to a small amount of stagnant areas. For the same reason, the increase of the dispersion coefficients in the real network for large  $Pe_n$  is similar to that for  $\rho'=12$ , whereas  $D_{||}^*$  for  $\rho'=4$  increases faster and eventually catches up with  $D_{||}^*$  for  $Pe_n$  larger than 100. In both types of hexagon networks the transition from the regime described by equation (35) to the regime described by equation (36) takes place for a much larger Péclet number than in the real network. This may result in part from the injection conditions and from the limited spatial and time ranges of the dispersion process.

## 8. Concluding Remarks

This study represents a step toward the quantification of geometrical properties and of transport processes in real fracture networks. It shows the practical difficulties of data acquisition and of their subsequent use in a quantitative way.

In this paper, results have been presented on the geometrical and topological properties of the real network. Possibly, the most important conclusion is that a simple model of randomly oriented monodisperse hexagons often yields the right order of magnitude for many properties. It would be interesting to try to extend this work by the analysis of the results relative to a network composed of two families as is the real network.

Finally, the transport properties derived here could not be compared to any real data obtained on the same block since such measurements were not performed by Ledéseret et al. [1993] before sample dissection. It would be extremely useful to perform such measurements on another block, and this would allow more detailed simulations and comparison.

**Acknowledgments.** One of us (O.H.) thanks the Research Council of Norway for financial support. Most computations were performed at CINES (subsidized by the MENESR) whose support is gratefully acknowledged.

## References

- Abelin, H., L. Birgersson, J. Gidlund and I. Neretnieks, A large-scale flow and tracer experiment in granite, 1, Experimental design and flow distribution, *Water Resour. Res.*, **27**, 3107-3117, 1991.
- Adler, P.M., *Porous Media*, Butterworth-Heinemann, Woburn, Mass., 1992.
- Adler, P.M., and J.-F. Thovert, *Fractures and Fracture Networks*, Kluwer Acad., Norwell, Mass., 1999.
- Balberg, I., C.H. Anderson, S. Alexander, and N. Wagner, Excluded volume and its relation to the onset of percolation, *Phys. Rev. B*, **30**, 3933-3943, 1984.
- Barrett, L.K. and C.S. Yust, Some fundamental ideas in topology and their application to problems in metallography, *Metallography*, **3**, 1-33, 1970.
- Barthélémy, P., Etude de la géométrie des réseaux de fractures naturelles à différentes échelles, Ph.D. thesis, Univ. Paris, 1992.
- Barthélémy, P., C. Jacquin, J. Yao, J.-F. Thovert, and P.M. Adler, Hierarchical structures and hydraulic properties of a fracture network in the Causse of Larzac, *J. Hydrol.*, **187**, 237-258, 1996.
- Berkowitz, B., and P.M. Adler, Stereological analysis of fracture network structure in geological formations, *J. Geophys. Res.*, **103**, 15,339-15,360, 1998.
- Billaux, D., J.P. Chiles, K. Hestir, and J. Long, Three-dimensional statistical modelling of a fractured rock-mass - an example from the Fanay-Augères mine, *Int. J. Rock Mech. Min. Sci. Geomech. Abstr.*, **26**, 281-299, 1989.
- Brenner, H., Dispersion resulting from flow through spatially periodic porous media, *Philos. Trans. R. Soc. London*, **297**, 81-133, 1980.
- Coats, K.H., and B.D. Smith, Dead-end pore volume and dispersion in porous media, *Soc. Pet. Eng. J.*, **4**, 73-84, 1964.
- Genter, A., H. Traineau, C. Dezayes, P. Elsass, B. Ledesert, A. Meunier, and T. Villemin, Fracture analysis and reservoir characterization of the granitic basement in the HDR Soultz Project (France), *Geotherm. Sci. Technol.*, **4**, 189-214, 1995.
- Gertsch, L.S., Three-dimensional fracture network models from laboratory-scale rock samples, *Int. J. Rock Mech. Min. Sci. Geomech. Abstr.*, **32**, 85-91, 1995.
- Gervais, F., Modélisation géométrique d'un réseau de fractures dans un massif rocheux stratifié, application aux carrières marbrières de Comblanchien, Ph.D. thesis, Ecole Nationale Supérieure des Mines, Paris, 1993.
- Huseby, O., J.-F. Thovert, and P.M. Adler, Geometry and topology of fracture systems, *J. Phys. A*, **30**, 1415-1444, 1997.
- Koestler, A.G., and K. Reksten, Insight into the 3D fracture network of an exposed analogue of fractured chalk reservoirs - the Lägerdorf case, paper presented at Fourth North Sea Chalk Symposium, Joint Chalk Research Program, Deauville, France, 1992.
- Koudina, N., R. Gonzalez Garcia, J.-F. Thovert, and P.M. Adler, Permeability of three-dimensional fracture networks, *Phys. Rev. E*, **57**, 4466-4479, 1998.
- Ledéseret, B., J. Dubois, B. Velde, A. Meunier, A. Genter, and A. Badri, Geometrical and fractal analysis of a three-dimensional hydrothermal vein network in a fractured granite, *J. Volcanol. Geotherm. Res.*, **56**, 267-280, 1993.
- Montemagno, C.D., and L.J. Pyrak-Nolte, Porosity of natural fracture networks, *Geophys. Res. Lett.*, **22**, 1397-1400, 1995.
- Mourzenko, V.M., J.-F. Thovert, and P.M. Adler, Permeability of a single fracture: Validity of the Reynolds equation, *J. Phys. II*, **5**, 465-482, 1995.
- Narr, W., and I. Lerche, A method for estimating subsurface fracture density in core, *AAPG Bull.*, **68**, 637-348, 1984.
- Odling, N.E., Network properties of a two-dimensional natural fracture pattern, *Pure Appl. Geophys.*, **138**, 95-114, 1992.
- Pyrak-Nolte, L.J., C.D. Montemagno, and D.D. Nolte, Volumetric imaging of aperture distributions in connected fracture networks, *Geophys. Res. Lett.*, **24**, 2343-2346, 1997.
- Rouleau, A., and J.E. Gale, Statistical characterization of the fracture system in the Stripa granite, Sweden, *Int. J. Rock Mech. Min. Sci. Geomech. Abstr.*, **22**, 353-367, 1985.

- Sahimi, M., Flow phenomena in rocks: From continuum models to fractals, percolation, cellular automata, and simulated annealing, *Rev. Mod. Phys.*, *65*, 1393-1534, 1993.
- Sahimi, M., B.D. Hughes, L.E. Scriven, and H.T. Davis, Dispersion in flow through porous media, I, One phase flow, *Chem. Eng. Sci.*, *41*, 2103-2122, 1986.
- Sallés, J., J.-F. Thovert, R. Delannay, L. Prevors, J.-L. Auriant, and P.M. Adler, Taylor dispersion in porous media. Determination of the dispersion tensor, *Phys. Fluids A*, *5*, 2348-2376, 1993.
- Snow, D.T., Anisotropic permeability of fractured media, *Water Resour. Res.*, *5*, 1273-1289, 1969.
- Vignes-Adler, M., A. Le Page, and P.M. Adler, Fractal analysis of fracturing in two African regions, from satellite imagery to ground scale, *Tectonophysics*, *196*, 69-86, 1991.
- 
- P. M. Adler, IPGP, tour 24, 4 Place Jussieu, F-75252 Paris Cedex 05, France. (adler@ipgp.jussieu.fr)
- R. Gonzalez-Garcia, and J.-F. Thovert, LCD-PTM, SP2MI, BP 30179, F-86962 Futuroscope Cedex, France. (thovert@lcd.ensma.fr)
- O. Huseby, IFE, Instituttveien 18, PO Box 40, N-2027 Kjeller, Norway. (olafh@ife.no)
- B. Ledésert, LGD, Bât. SN5, Université de Lille I, F-59650 Villeneuve d'Ascq Cedex, France. (beatrice.ledesert@univ-lille1.fr)

(Received May 4, 1999; revised February 18, 2000; accepted April 19, 2000.)